Atmospheric Research 239 (2020) 104924

Contents lists available at ScienceDirect

Atmospheric Research

journal homepage: www.elsevier.com/locate/atmosres

Vertical profiles of droplet size distributions derived from cloud-side observations by the research scanning polarimeter: Tests on simulated data

Mikhail D. Alexandrov[a,b,*], Daniel J. Miller[c], Chamara Rajapakshe[d,c], Ann Fridlind[b], Bastiaan van Diedenhoven[e,b], Brian Cairns[b], Andrew S. Ackerman[b], Zhibo Zhang[d]

[a] Department of Applied Physics and Applied Mathematics, Columbia University, 2880 Broadway, New York, NY 10025, USA
[b] NASA Goddard Institute for Space Studies, 2880 Broadway, New York, NY 10025, USA
[c] NASA Goddard Space Flight Center, Greenbelt, MD 20771, USA
[d] Department of Physics, University of Maryland, Baltimore County, 1000 Hilltop Cir, Baltimore, MD 21250, USA
[e] Center for Climate Systems Research, Columbia University, 2880 Broadway, New York, NY 10025, USA

ARTICLE INFO

Keywords:
Clouds
Remote sensing
Cloud droplet size
Vertical profile
Radiometry
Polarization

ABSTRACT

The Research Scanning Polarimeter (RSP) is an airborne along-track scanner measuring the polarized and total reflectances with high angular resolution. It allows for accurate characterization of liquid water cloud droplet sizes using the rainbow structure in the polarized reflectance. RSP's observations also provide constraints on the cumulus cloud's 2D cross section, yielding estimates of its geometric shape. In this study for the first time we evaluate the possibility to retrieve vertical profiles of microphysical characteristics along the cloud side by combining these micro- and macrophysical retrieval methods. First we constrain cloud's geometric shape, then for each point on the bright side of its surface we collect data from different scans to obtain the multi-angle polarized reflectance at that point. The rainbow structures of the reflectances from multiple points yield the corresponding droplet size distributions (DSDs), which are then combined into vertical profiles. We present the results of testing the proposed profiling algorithm on simulated data obtained using large eddy simulations and 3D radiative transfer computations. The virtual RSP measurements were used for retrieval of DSD profiles, which then were compared to the actual data from the LES-model output. A cumulus congestus cloud was selected for these tests in preparation for analysis of real measurements made during the Cloud, Aerosol and Monsoon Processes Philippines Experiment (CAMP^{2}Ex). We demonstrate that the use of the non-parametric Rainbow Fourier Transform (RFT) allows for adequate retrieval of the complex altitude-dependent bimodal structure of cloud DSDs.

1. Introduction

Cloud feedbacks remain the most uncertain radiative feedbacks in climate models and there continue to be large uncertainties in the estimates of the forcings associated with aerosol-cloud interactions (e.g., Boucher et al., 2013; Flato et al., 2013). In addition to providing data for understanding of cloud processes themselves, accurate and robust remote sensing estimates of droplet sizes for different cloud types (especially for broken clouds) are also crucial for studies of the interactions between clouds and aerosols.

This study based on computer-simulated clouds, 3D radiation fields, and remote-sensing observations was conducted in preparation to Cloud, Aerosol and Monsoon Processes Philippines Experiment (CAMP^{2}Ex). This is NASA airborne campaign held in August – September 2019 with the main goal of characterizing the role played by atmospheric aerosols in modulating the frequency and amount of warm and mixed-phase precipitation in the vicinity of the Philippines during the Southwest Monsoon. One of the NASA focus area in this campaign is examination of the aerosol effects on the optical and microphysical properties of shallow cumulous and congestus clouds, and how, ultimately, these effects relate to the transition from shallow trade wind cumuli to the high-altitude deep convective clouds (e.g., precipitating cumulonimbus). Cumulus congestus (or towering cumulus, Tcu) clouds, being the middle mode of the trimodal distribution of tropical cloud types (see, e.g., Johnson et al., 1999) play a fundamental role in this transition (see, e.g., Waite and Khouider, 2010, and references therein). Greater concentrations of aerosol particles may lead to more frequent development of congestus clouds above the freezing level (e.g., Li et al.,

* Corresponding author at: Department of Applied Physics and Applied Mathematics, Columbia University, 2880 Broadway, New York, NY 10025, USA.
E-mail address: mda14@columbia.edu (M.D. Alexandrov).

https://doi.org/10.1016/j.atmosres.2020.104924
Received 2 July 2019; Received in revised form 13 February 2020; Accepted 20 February 2020
Available online 25 February 2020
0169-8095/

2010; Sheffield et al., 2015), however, uncertainties in updraft physics sill remain very large (e.g., Ackerman et al., 2015; Fridlind et al., 2017; Ladino et al., 2017).

In this study we introduce a novel technique for characterization of cumulus (and Tcu, in particular) cloud structure by means of multi-angular polarimetric passive remote sensing. This method uses observations by the airborne Research Scanning Polarimeter (RSP), which was deployed during CAMP^{2}Ex onboard the NASA P−3B aircraft. The RSP is an along-track scanner measuring the polarized and total reflectances in nine spectral channels. Its unique angular resolution coupled with the high frequency of measurements allows for accurate characterization of liquid water cloud droplet sizes using the rainbow (cloud bow) structure, which is observed in the polarized reflectance over the scattering angle range from 135° to 165°. RSP's observations also provide geometric constraints on the cumulus cloud's 2D cross section between a number of tangent lines of view, yielding estimates of the cloud's macroscopic parameters, such as its geometric shape, dimensions, and height above the ground (Alexandrov et al., 2016b). Multiple cloud layer heights also can be derived from RSP data using a block-matching stereoscopic technique (Sinclair et al., 2017). Detailed descriptions of the RSP measurements and retrieval techniques are presented in Sections 2 and 3.

Passive remote sensing techniques (including those using RSP measurements) are generally expected to provide information only about cloud-top microphysical properties. Our RSP-based retrievals of droplet size distributions (DSDs) from past deployments demonstrated strong consistency with the correlative in situ data collected within 50 m of cloud top (Alexandrov et al., 2018). However, especially in the case of cumulus congestus clouds, knowledge on the cloud boundaries and vertical microphysical structure is key for understanding cloud evolution and radiative properties (which can be influenced by e.g., dry air entrainment and radiative cooling at cloud sides). Currently characterization of cloud vertical structures is limited to in situ measurements (which are sparse) and radar reflectivities (which have only limited information content about DSDs). In this situation development of retrieval techniques allowing multi-angle passive measurements to provide additional information on cloud shape and vertical structure of microphysical properties may have a great potential. These techniques, however, need to be evaluated using collocated in situ and radar measurements.

In this study for the first time we evaluate the possibility to use RSP observations for retrieval of vertical profiles of microphysical characteristics along the illuminated side of the cumulus cloud. This task requires a combination of our previously developed micro- and macrophysical retrieval methods. First, we use RSP's view-lines tangent to the cloud surface to determine its shape. Then for each point on the bright side of this surface we aggregate view-lines passing through it thereby constructing the polarized reflectance as a function of scattering angle corresponding to that point. The rainbow structure of this reflectance is then analyzed yielding the droplet size distribution at that point. Finally, the retrievals made for all available points at the cloud surface are combined into vertical profiles of the DSDs and their parameters. We will illustrate the proposed profiling algorithm and evaluate its performance on simulated data. For this purpose we performed 3D radiative transfer (RT) computations on a LES-modeled Tcu cloud then sampled the resulting RT dataset to emulate “virtual RSP measurements” made at a certain flight altitude above the cloud. These “measurements” were analyzed and the retrieved profiles were compared to the actual data from the LES-model output. We will show that the use of non-parametric Rainbow Fourier Transform (RFT) allows for adequate capture of the complex altitude-dependent bimodal structure of Tcu's DSDs, thus, paving the way for RSP-based process-oriented cloud remote sensing.

2. The research scanning polarimeter: measurements and retrieval methods

The RSP (Cairns et al., 1999) is an along-track scanning polarimeter, which scans its 14-mrad field of view in a meridional plane taking samples at 0.8° intervals within ± 60° from the normal (about 150 measurements per scan). The spectral bands of this instrument are centered at 410, 470, 550, 670, 865, 960, 1590, 1880, and 2260 nm. The RSP measurements made simultaneously in each of these channels are converted into the I, Q, and U components of the Stokes vector (Hansen and Travis, 1974; Mishchenko et al., 2006) and further into the total and polarized reflectances. The Stokes vector components, initially defined with respect to the scan plane of the instrument, are rotated (see Hansen and Travis, 1974) into the scattering plane (the plane containing both solar and view directions).

The vast volume of the RSP's measurements made at a variety of positions and viewing angles allows for characterization of both microphysical (cloud droplet size distributions) and macrophysical (cloud shape and position) properties. Depending on the type of the retrieval, specific measurements from different scans are grouped together (aggregated). In particular, determination of the DSD at a certain point along the cloud surface requires aggregation of polarized reflectances from all RSP's lines of view passing through this point (see, e.g., Alexandrov et al., 2012a). On the other hand, characterization of the cumulus cloud shape (Alexandrov et al., 2016b) is made using all available view-lines tangent to the cloud surface. Here “tangent” is determined using a threshold in total reflectance separating clear-sky views from those obstructed by cloud. The idea behind this study is to combine these two retrieval techniques into one providing spatially resolved cloud microphysics profiles with the focus on characterization of cloud processes.

While the RSP measurements facilitate radiometric (Nakajima-King type) inversions (Nakajima and King, 1990; Platnick, 2000), the most robust retrievals of cloud DSDs from its data are based on polarized reflectance measurements in the rainbow (cloud bow) scattering range between 135° and 165° (Bréon and Goloub, 1998; Bréon and Doutriaux-Boucher, 2005; Alexandrov et al., 2012a, 2016b, 2015, 2016a, 2018; Shang et al., 2015, 2019). The rainbow is a sharply-defined oscillatory feature in polarized reflectance with frequency depending on the droplet size (larger frequencies for larger droplets) and the amplitude reflecting the width of the DSD (smaller amplitudes for wider distributions). The rainbow shape is largely determined by single scattering of light by cloud droplets. This allows us to avoid the retrieval uncertainties associated with 3D effects as well as unknown surface albedo, aerosol loadings, and amounts of ice over or mixed with liquid water layers. For the same reason the retrievals are accurate even for low cloud optical thicknesses (COTs), down to about unity. The single-scattering nature of the rainbow structure makes the RSP retrievals representative of the cloud layer within about 50 m from its surface (Alexandrov et al., 2012a, 2018). Such localization of RSP-derived cloud microphysical properties (rather than weighted characteristics of the full cloud profile as is the case in Nakajima-King-type inversions (Platnick, 2000)) facilitates validation of remote-sensing retrievals by comparison with direct in situ measurements made at cloud surface. A recent validation study (Alexandrov et al., 2018) demonstrated good agreement (better than within 1 μm in effective radius and in most cases better than within 0.02 in effective variance) between the RSP retrievals and co-located in situ measurements made during the North Atlantic Aerosols and Marine Ecosystems Study (NAAMES, https://naames.larc.nasa.gov/) in May–June 2016.

We currently use two different algorithms for cloud DSD characterization based on polarized rainbow structure. The first method is a parametric fit technique (Alexandrov et al., 2012a) based on the earlier works by Bréon and Goloub (1998) and Bréon and Doutriaux-Boucher (2005). This method uses a look-up table (LUT) pre-computed according to Mie theory for arrays of the effective radius (r_{eff}) and

variance (v_{eff}) (Hansen and Travis, 1974) of the cloud droplet size distribution, which is assumed to have a gamma-distribution shape. The second retrieval algorithm, the Rainbow Fourier Transform (RFT) (Alexandrov et al., 2012b)) is a non-parametric method capable to derive the entire shape of the droplet area (or cross section) distribution (DAD)

$$n_a = \frac{r^2\ n(r)}{\int_0^\infty r^2\ n(r)\ \mathrm{d}r} \tag{1}$$

(where $n(r)$ is the corresponding DSD) without any a priori assumptions. The shape of the RFT-derived DAD is analyzed and interpreted by fitting it with a number of gamma-distribution-shaped modes (see Alexandrov et al., 2015, for details). The effective radius and variance of each DAD mode are then converted to the respective parameters of the corresponding DSD mode (which also has the gamma-distribution shape) using analytical relationships. While the RFT provides more detailed information about cloud DSD than the parametric fit in multimodal cases, it has higher sensitivity to measurement imperfections (e.g., incomplete angular range, inaccurate aggregation, etc.), which results in oscillatory artifacts in the retrieved DAD shape. The parametric fit is more stable in response to measurement shortcomings, so simultaneous use of both methods leads to a more robust picture. For monomodal DSDs both methods give the same results.

In our previous work we have retrieved bimodal and multimodal DSDs with the modes corresponding to distinct cloud layers (Alexandrov et al., 2015, 2016a, 2018). However, in the case of Tcu cloud presented below, the bimodality of the observed and actual DSDs is caused by the presence of two different populations of droplets within the same microphysical volumes.

Alexandrov et al. (2016b) introduced technique for cloud shape characterization which is simpler than the traditional stereoscopy and is not affected by absence of distinct features in the cloud shape. It relies on the collection of all available scanner's view-lines specified to be tangent to the cloud surface (based on a simple threshold in total reflectance which yields a 1D cloud mask). Together, these lines form a polygon enclosing the cloud's cross-section that can be used as a proxy for the cloud shape.

3. LES model and 3D radiative transfer algorithm

The results of this study were obtained using an atmospheric LES code developed for boundary layer clouds, the Distributed Hydrodynamic Aerosol and Radiation Model Application (DHARMA; Stevens and Bretherton, 1996; Stevens et al., 2000, 2002; Ackerman et al., 2004; Kirkpatrick et al., 2006; Zhang et al., 2012; Miller et al., 2016)). DHARMA simulations have 142.86-m horizontal and 100-m vertical resolution (within the altitude range 1–14 km that we are interested in) and include prognostic multi-modal aerosol (with sinks, but without sources). The model's output provides spatially resolved cloud droplet number concentrations sampled in 50 bins according to droplet size. The bin size increases with the droplet radius, which varies between 1 μm and 3.6 mm, so such DSDs can include drizzle mode. In our case the DSDs appeared to be identically zero for droplet sizes exceeding 30 μm.

The 3D radiative transfer in this study is performed using the Multiple-Scaling-based Cloudy Atmospheric Radiative Transfer (MSCART) algorithm (Wang et al., 2017). MSCART is a Monte Carlo algorithm that solves the integral radiative transfer equation in a cloudy atmosphere rapidly and accurately. The DHARMA-derived 50-bin DSDs are directly used as input for MSCART, without replacing them with simplified analytical DSDs having the same r_{eff} and v_{eff}. A long-standing problem in Monte Carlo radiative transfer calculations is that simulations involving large particles (i.e., cloud droplets), which have highly forward-peaked scattering phase functions, converge very slowly to a low-noise (also called “low-variance”, which should not be confused with the DSD's variance) solution even after numerous samples (Barker et al., 2003; Iwabuchi, 2006; Iwabuchi and Suzuki, 2009). This is because such media rarely scatter into the direction of interest (e.g., the detector) compared to the number of simulated scattering events in forward direction. MSCART addresses the computational expense of simulation in a cloudy atmosphere by implementing a hybrid of two variance-reduction methods (VRM) in a scattering-order dependent framework. The first VRM implemented is an order-dependent phase function forward truncation (OPFFT), which reduces the fraction of photons that are forward-scattered as a function of scattering order. Thus for higher-order scattering events the algorithm increases the computation efficiency without harming the accurate representation of the phase function for lower-order scattering. This is particularly important for accurate polarimetric results, because the polarized reflectance of clouds is dominated by low-order scattering (Bréon and Goloub, 1998). The second VRM is order-dependent Target Directional Importance Sampling (OTDIS). This method (Buras and Mayer, 2011) artificially increases the probability of scattering into directions of interest, which is an essential feature for modeling reflectances for instruments that have narrow instantaneous fields of view (such as lidars and the RSP). This is accomplished by creating “cloned photons” from a scattered “mother photon” during each scattering event. The cloned photon scatters have a modified phase function that encourages scattering into the detector direction, while the mother photons scatter according to the normal physical process and create new cloned photons at each scattering event. Each cloned photon undergoes its own multiple scattering calculation, with contribution into the detector direction computed at each step. The weight of each cloned photon is reduced by a correction factor, accounting for the true probability of scattering into the detector direction. While the OTDIS approach provides a low-variance solution, it can be inefficient by itself because of the large number of multiple scattering calculations performed for each cloned photon. The purpose of the implementation of OTDIS in MSCART is primarily to reduce the variance for low-order scattering events, which have little to no variance reduction from the OPFFT VRM. As a consequence the number of cloned photons produced by MSCART is reduced with increasing scattering order, thus, providing variance reduction for low-order scattering and the efficiency for higher-order scattering. The efficiency and accuracy of MSCART makes it an ideal 3D RT algorithm for computing both total and polarized reflectances in complex LES-derived cloud domains. MSCART has successfully demonstrated this capability during participation in the International Polarized Radiative Transfer (IPRT) intercomparison project (Emde et al., 2018).

4. Case of cumulus congestus cloud

4.1. Simulated cloud

Initial tests of our droplet size profiling technique were performed on the simulations earlier used by Alexandrov et al. (2016b). They were produced using the 3D radiative transfer model MYSTIC (Monte Carlo code for the phYSically correct Tracing of photons In Cloudy atmospheres (Mayer, 2009; Emde et al., 2010)) applied to LES-generated shallow, maritime convection (Ackerman et al., 2004). However, in preparation to CAMP^{2}Ex field campaign, we decided to illustrate the cloud profiling algorithm and to evaluate its performance using newly-simulated cumulus congestus cloud, which is typical for the oceans surrounding Philippines during the monsoon season. This particular cloud (Fig. 1 (top)) was taken from DHARMA simulations based on the observations made over the Gulf of Mexico in August – September 2013 during another field campaign: Studies of Emissions and Atmospheric Composition, Clouds and Climate Coupling by Regional Surveys (SEAC^{4}RS). We selected a Tcu cloud at an early stage of its development, before it develops the characteristic “anvil” – the ice-phase top,

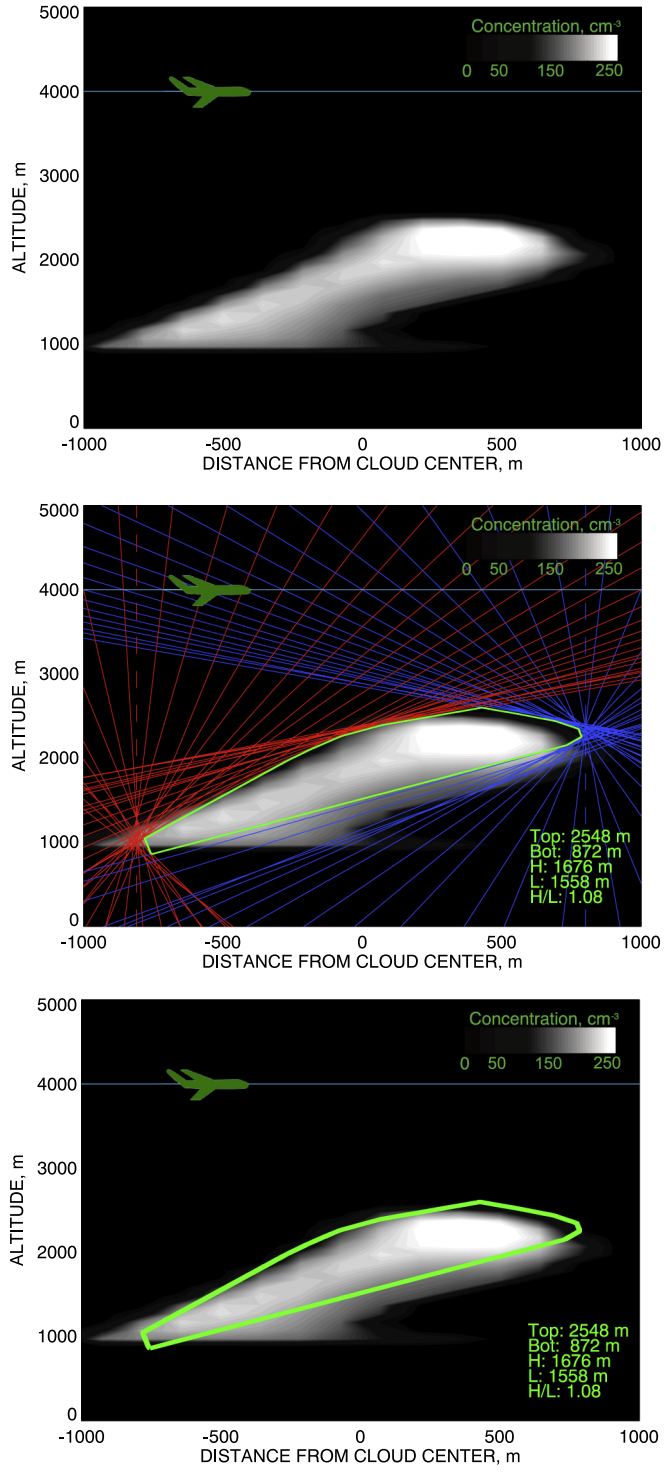

Fig. 1. Determination of the shape of simulated Tcu cloud using virtual RSP measurements. Top: LES-simulated cloud droplet density. Middle: RSP view-lines tangent to the cloud surface during overflight. Bottom: the derived (polygon) cloud shape. Blue line with airplane icon indicates the flight altitude. (For interpretation of the references to colour in this figure legend, the reader is referred to the web version of this article.)

because this feature can obscure the shape of the liquid-water-phase cloud body from the view of the instrument flown above the cloud.

4.2. 3D RT model setup and cloud shape

The solar zenith angle in the RT run was set to 60° with the Sun illuminating the cloud from the left in Fig. 1 at 863-nm wavelength. The altitude of the virtual RSP was chosen to be 4 km (1.5 km above cloud top). This relatively low observation altitude allows for sufficient number of RSP view-lines grazing cloud top and bottom, thus, capable to constrain their heights (as it is seen in Fig. 1 (middle)). The distances between subsequent points at which RSP-like scans (within ± 60° from nadir) were collected was 100 m. These points can be seen in Fig. 1 (middle) as intersections of red and blue lines at the aircraft altitude (light-blue line). Combination of all view-lines tangent to the cloud surface yields a polygon representing the cloud cross-section shape shown in Fig. 1 (bottom) by the thick green line. Confirming our visual perception of the cloud in Fig. 1 (top), this polygon depicts a rather "leaning tower" cloud shape confined between roughly 1 and 2.5 km altitude. We understand that real (and LES) cloud shapes are not polygons with smooth boundaries but have rather "fluffy" structure. In order to make RSP-derived cloud shapes more realistic we proposed in our earlier paper (Alexandrov et al., 2016b) a second step of the procedure where a number of disks are inscribed within the polygon constructed on the first step, and the union of these disks is called the final cloud shape. The resulting cloud shapes look similar to the schematic cloud drawings in Fig. A.1 in the Appendix A of this paper. However, in the case of Tcu cloud at hand this second-step procedure was found to be inefficient (due to elongated cloud shape) and is not implemented here. At the same time, the polygon itself appears to be a good approximation of the cloud shape, especially on the bright side, which is almost linear (see Fig. 1 (bottom)). While the entire notion of "cloud boundary" is not well-defined (cloud is a collection of droplets, not a solid object) it is difficult to quantify the accuracy of our shape retrievals. In some cases our algorithm has difficulties. For example, the shape that was "cut out" along straight lines is always convex, so any concave feature in the cloud (e.g., small depression on the bright side at about 2000 m altitude in Fig. 1) cannot be detected. Also, characterization of horizontal parts of the cloud boundary (cloud top and bottom) is always a challenge since it relies on RSP views from large distances. Errors in determination of the cloud boundary may result in misattribution of the polarized signal (dominated by single scattering) to a wrong scattering point, thus, affecting the rainbow structure and, therefore, DSD retrievals. Having this in mind, we do not include points where cloud boundary location is questionable into detailed comparisons with LES DSDs presented in Section 4.5. Note, however, that for real RSP measurements aggregation at cloud top can be made using our standard block-correlation stereo technique (Sinclair et al., 2017) since real clouds have sharply-defined features (while relatively smooth LES-modeled clouds lack such features). Finally, we should note that the specific size and shape of the RSP-derived polygon depends on the brightness threshold chosen by the researcher to single out the cloudy part of the 1D cloud mask within each single RSP scan. As it was discussed in detail by Alexandrov et al. (2016b), this optical threshold reflects both physical parameters (such as droplet density in the cloud) and viewing geometry (e.g. solar and viewing angles, bright or shadowy side of the cloud), and does not necessarily directly correspond to a specific physical threshold (e.g., in number concentration of cloud droplets). This introduces a degree of subjectivity in definition of "cloud boundary", which, however, does not preclude meaningful measurement results, as we will show below.

4.3. Derivation of droplet size profile

Fig. 2 outlines the aggregation of the view-lines from different RSP scans (shown in green) corresponding to a single point on the illuminated cloud side and belonging to the rainbow scattering range (135° – 165°). The direction to the Sun is depicted by yellow line, while the whole range of points at the cloud surface used for derivation of the vertical profile of droplet sizes is shown in red. The polarized rainbows corresponding to the points on this red curve were analyzed using both the parametric fit method (yielding the vertical profiles of the effective

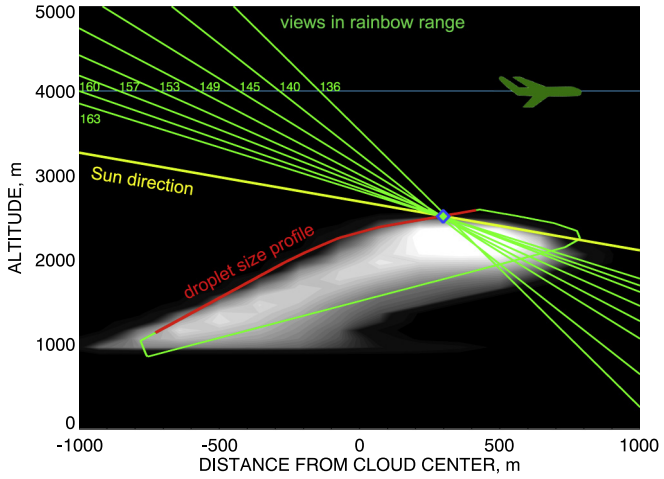

Fig. 2. Geometrical scheme for collecting RSP's view-lines forming the polarized rainbow (within 135°–165° in scattering angle) for a point at the cloud surface (the latter is constrained by the procedure outlined in Fig. 1).

radius and variance of the pre-assumed gamma-distribution DSD) and by the RFT (providing full DAD shapes, which can be decomposed into several gamma-distribution modes). Note that by the nature of the RSP measurements a "photon" coming to the detector from the direction of a certain aggregation point may not necessarily be scattered at this particular point but at any point on the ray going from the detector in this direction. This may introduce some kind of averaging of the retrieval results over neighborhood of the aggregation point. We induce further averaging by inclusion in the rainbow shape measurements from additional directions pointing to not exactly the aggregation point but to other points close to it. These directions have tangents of their viewing angles within 0.03 from that of the direction to the initial aggregation point. While blurring somehow the spatial picture, this allows us to increase the number of data points in the rainbow curve, thus, facilitating more accurate analysis of its shape.

The profiles of the effective radius and variance derived using the parametric fit method are shown in Fig. 3 (left and right, respectively) by red curves in comparison with their LES-DSD counterparts (blue curves). For these plots we took the RSP retrievals for every point from the profiled part of cloud boundary (which is defined with 1-m resolution) and coupled them with the LES-DSD parameters from the nearest LES grid points. Effective radii and variances for LES model are computed by direct integration of the DSDs (see Hansen and Travis, 1974) at each selected grid point. These points are sparser than the RSP aggregation points corresponding to them that results in some repetition of LES-derived values (vertical segments in blue curves). The comparisons show good agreement between actual and measured values: within 1–2 μm for r_{eff} and 0.02–0.05 for v_{eff}. Rather small, however systematic, overestimation of both r_{eff} (below 2.3 km altitude) and v_{eff} by the RSP may be caused by averaging of the RSP signal over multiple scattering points (especially those located deeper in the cloud than our boundary) in the RT computations. Fig. 4 (left) shows larger values of r_{eff} in the cloud interior than at its boundary in LES 2D cloud cross section. The influence of inclusion of larger droplets into averaging of the RSP signal is expected to widen the retrieved DSD and also bias it towards larger droplet sizes compared to LES DSD from a single point at the boundary.

Fig. 3 shows two distinctive regimes of DSD's evolution with altitude. In the first regime, the effective radius profile (Fig. 3 (left)) shows steady increase in droplet size from r_{eff} of 9–10 μm at cloud bottom (1.2-km altitude) to 13–15 μm at around 2.2 km. At the same altitude range the effective variance stays generally constant within 0.05–0.10 range (with RSP retrievals showing somehow larger values than LES). In the next regime, taking place between 2.2-km altitude and cloud top at 2.6 km, r_{eff} falls sharply back to 9–10 μm, while v_{eff} rapidly increases to 0.25 value. The same behavior can be seen in Fig. 4 showing 2D contour plots of r_{eff} and v_{eff} values from LES-model output within the observed cloud cross-section (size of the pixels there represents the resolution of the LES model). These plots confirm sharp decrease in droplet size and increase of the DSD width near cloud top (and also in another area along the shadowy side of the cloud).

4.4. Bimodal droplet size distributions

In our previous studies (Alexandrov et al., 2015, 2016a, 2018), large values of the effective variance derived using the parametric-fit approach appeared to indicate that the DSD was actually bimodal (with two narrow modes, rather than a single wide mode). This was revealed by the non-parametric RFT retrievals of size distribution shapes and supported by correlative lidar and/or in situ measurements indicating in those cases a multi-layer structure of the observed cloud system. Using the RFT instead of the parametric fit yields a representative vertical profile (along the cloud edge) of the detailed droplet area distributions presented in Fig. 5 (left). This profile is in good qualitative

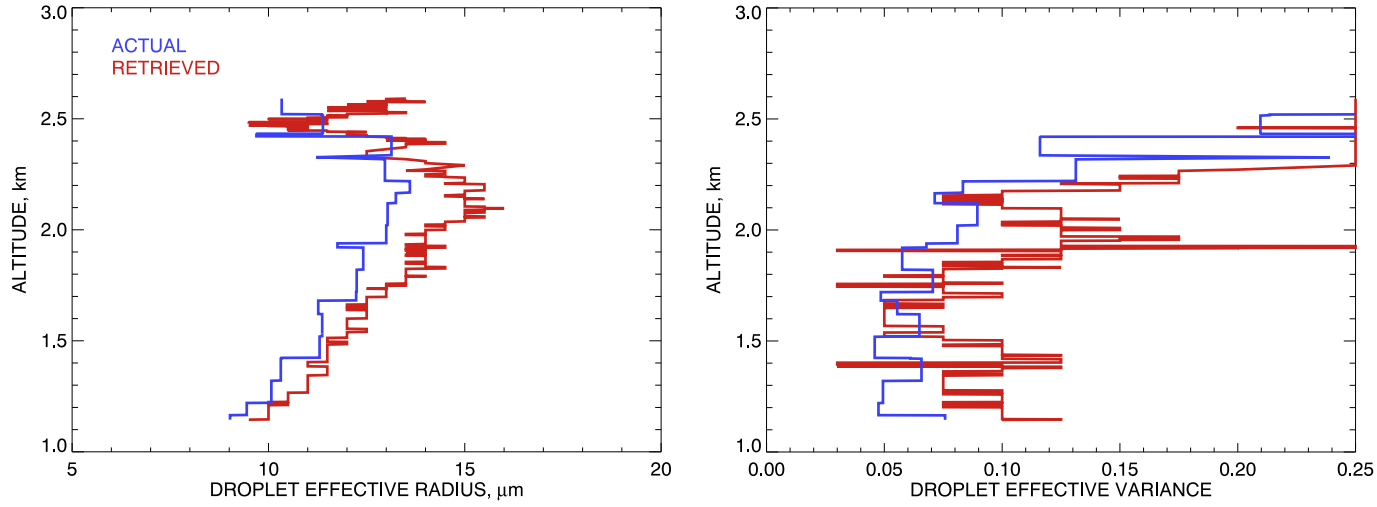

Fig. 3. Vertical profiles of effective radius (left) and variance (right) of droplet size distributions along the illuminated cloud side (red curve in Fig. 2). Blue curves show the actual values from LES model output, while red curves depict retrievals from virtual RSP measurements using the parametric fit method. (For interpretation of the references to colour in this figure legend, the reader is referred to the web version of this article.)

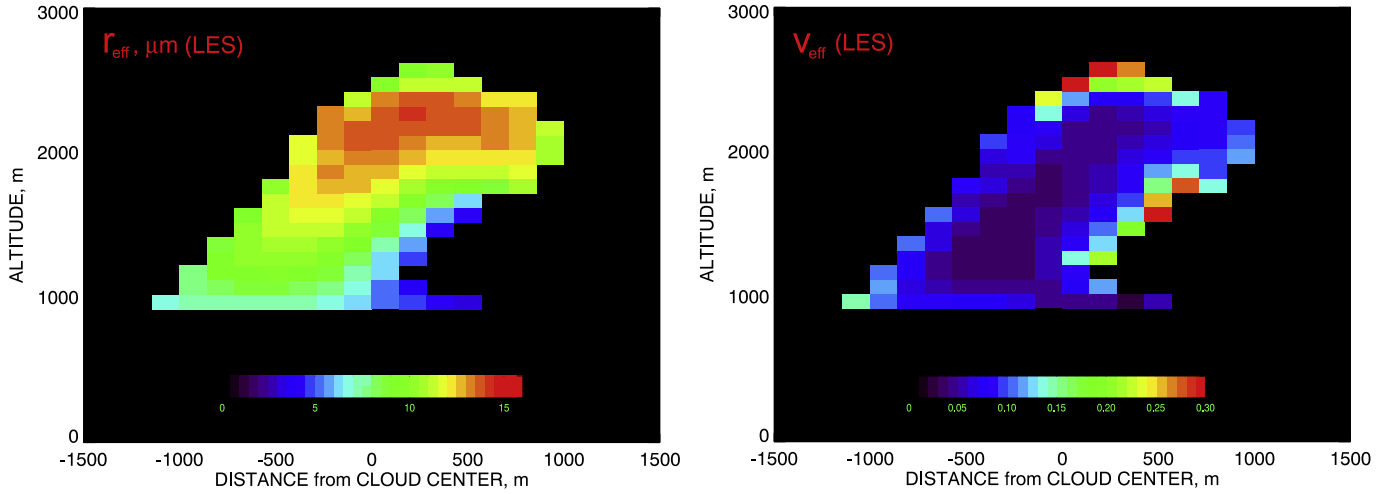

Fig. 4. Actual (from LES model) distribution of effective radius (left) and variance (right) values within the cloud cross-section being studied. The size of the pixels represents the resolution of the LES model.

agreement with its LES-model counterpart sampled (as in Fig. 3) at the LES grid points closest to the RSP aggregation points (Fig. 5 (right)). RSP DADs appear to be wider than their LES counterparts probably because of effective averaging over multiple LES grid points in the RT computations (discussed in Section 4.3).

These profiles provide a better understanding of the cloud's microphysical structure and the processes behind it than the profiles of the integral parameters – effective radius and variance – shown in Fig. 3. In particular, Fig. 5 reveals two distinctive DAD (and, therefore, DSD) modes. One of them, larger in droplet size, corresponds to the droplet population that originates at cloud bottom (1-km altitude) and is uplifted to the top (around 2.5-km altitude) while, due to condensation, its particles grow from approximately 5 to 15 μm in DAD's mode radius. (Note that the droplet area distributions in Fig. 5 are normalized to their maxima, so the brightest red points correspond to their mode radii.) Closer to cloud top this mode starts to disappear (more rapidly in RSP picture than in the LES one), probably due to collision-coalescence leading to gravitational removal. The other DAD-DSD mode corresponds to a small-droplet population (5 μm or less in mode radius) which becomes comparable in strength with the uplifted population within 2.3–2.5-km altitude range. This is consistent with secondary droplet activation above cloud base in the simulation, which can be promoted by e.g., accelerating updrafts (driving supersaturation higher) and precipitation formation (decreasing the surface area available to relieve supersaturation). This process may involve in-cloud nucleation of new droplets on aerosol particles that ascend within cloud updrafts along with cloud droplets (Segal et al., 2003). In this case new droplets are nucleated above the cloud base at the altitude where supersaturation in ascending cloud parcels exceeds the supersaturation maximum near the cloud base. An alternative explanation of bimodality of droplet size spectra (Lasher-Trapp et al., 2005) is based on entrainment of dry air, and its subsequent mixing into the cloud. This air may dilute the droplet population, shrink droplets by evaporation, and introduce additional cloud condensation nuclei into the cloud that may activate new droplets. Fig. 4 (right) shows the largest effective variances (indicating bimodality of the simulated DSDs) at cloud edges (top and side of the cross-section). This may actually support the entrainment-based explanation, since the updraft-driven droplet activation is expected to be stronger near the center of the cloud rather than at its edges.

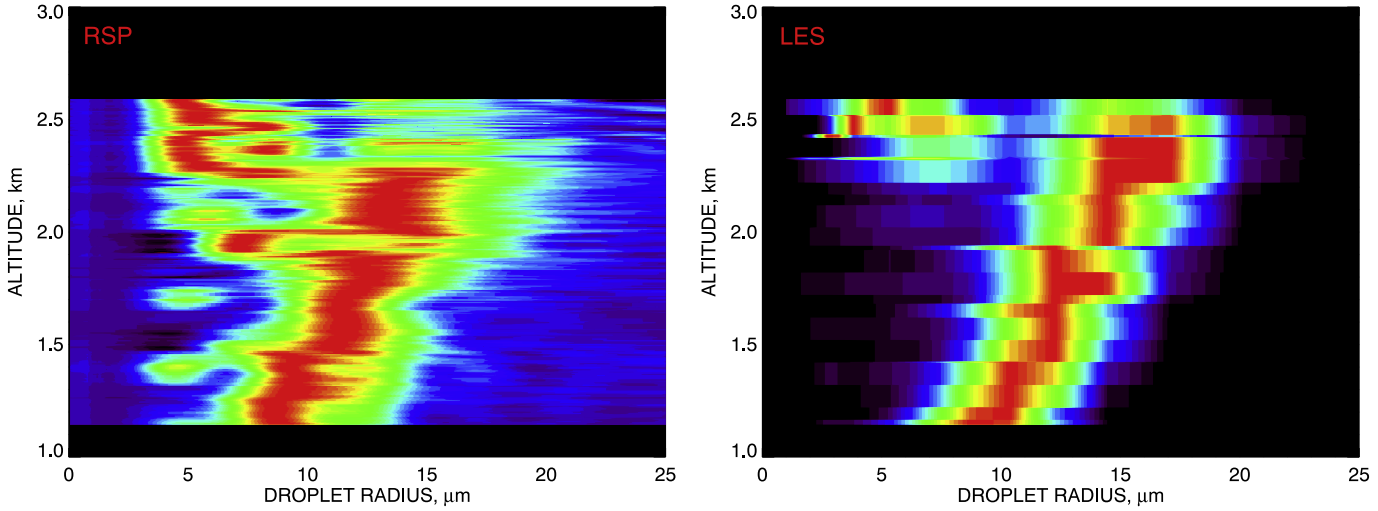

Fig. 5. The vertical profiles of droplet area distributions (normalized to their maxima) along the bright side of the cloud (highlighted in red in Fig. 2). Left: point-by-point RFT-based retrievals from virtual RSP observations. Right: actual distributions from the LES-model grid points nearest to the RSP aggregation points on the cloud side. Both plots clearly indicate presence of two separate droplet size modes: larger (growing in radius with altitude) and smaller (activated near cloud top). (For interpretation of the references to colour in this figure legend, the reader is referred to the web version of this article.)

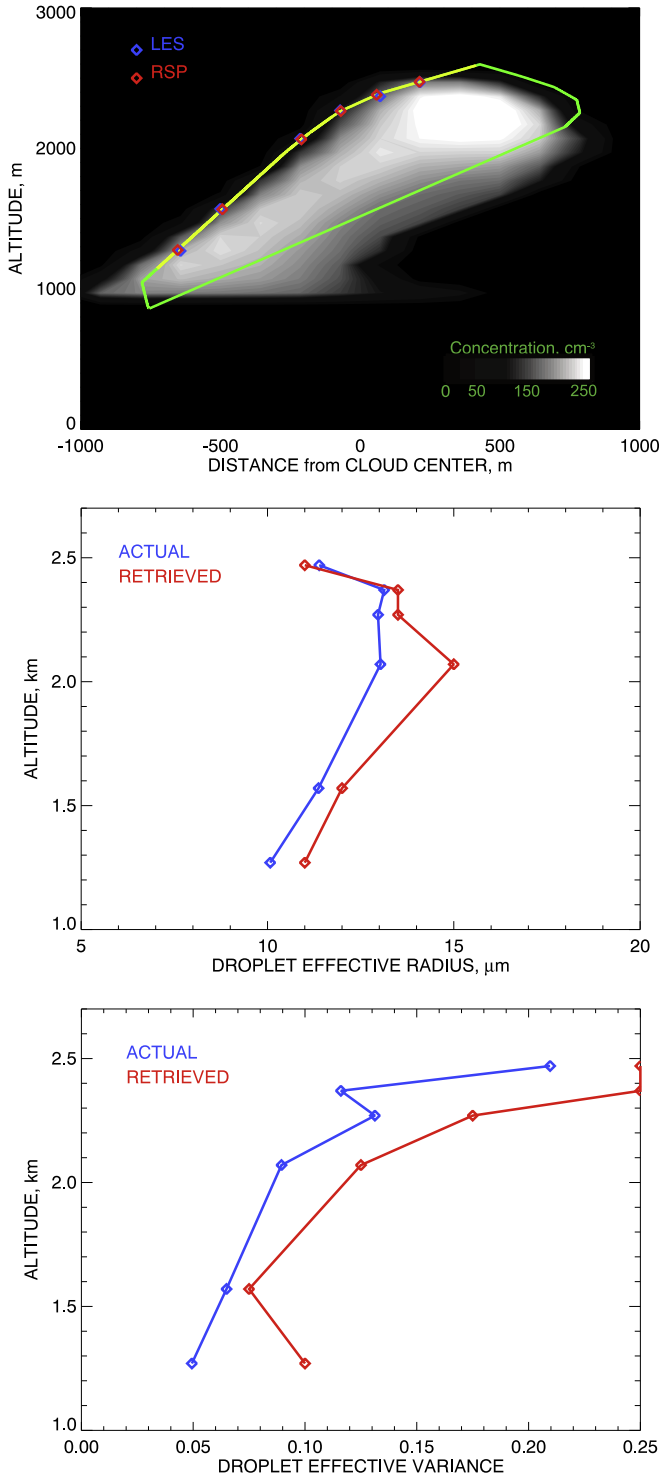

Fig. 6. Comparison between virtual-RSP retrievals and actual LES-model DSD parameters. Top: six LES grid points (blue diamonds) on the RSP-derived cloud "boundary" (green line) and the six RSP aggregation points closest to them (red diamonds); the RSP profile range is highlighted in yellow. Middle and bottom: profiles of the actual (blue) and retrieved (red) total effective radius (middle) and variance (bottom) at the points specified in top plot. The presented RSP retrievals are made using the parametric fit method. The values of the parameters plotted here are also presented in Table 1. (For interpretation of the references to colour in this figure legend, the reader is referred to the web version of this article.)

Table 1
Actual (LES) and retrieved (RSP) DSD parameters from Figs. 6 and 8.

Height	Total		Mode 1			Mode 2		
	r_{eff}, μm	v_{eff}	r_{eff}, μm	v_{eff}	weight	r_{eff}, μm	v_{eff}	weight
2470 m								
LES	11.4	0.21	4.0	0.03	0.14	18.1	0.07	0.86
RSP	11.0	0.25	9.9	0.23	0.91	17.5	0.01	0.09
2370 m								
LES	13.1	0.12	6.6	0.06	0.05	20.7	0.19	0.95
RSP	13.5	0.25	9.1	0.09	0.59	17.1	0.04	0.41
2270 m								
LES	13.0	0.13	8.6	0.14	0.41	15.0	0.02	0.58
RSP	13.5	0.18	10.7	0.17	0.70	18.6	0.05	0.30
2070 m								
LES	13.0	0.09	9.8	0.27	0.29	14.8	0.02	0.71
RSP	15.0	0.13	5.9	0.07	0.16	15.0	0.10	0.84
1570 m								
LES	11.4	0.06	8.5	0.03	0.10	12.5	0.03	0.91
RSP	12.0	0.08	7.1	0.02	0.07	12.2	0.05	0.93
1270 m								
LES	10.1	0.05	7.1	0.04	0.08	10.8	0.04	0.92
RSP	11.0	0.10	none	none	none	10.0	0.06	1.00

4.5. Detailed analysis at selected points

For more detailed quantitative analysis and comparison of the virtual RSP retrievals with their LES-model counterparts we selected six model's grid points (depicted by blue diamonds in Fig. 6 (top left)) along the RSP-derived cloud boundary sampled at the model's resolution (with one gap). For each of the selected LES points we picked the closest RSP data point (red diamonds in the same Figure). The profiles of model (blue) and retrieved (red) total effective radius and variance are presented in Fig. 6 (middle and bottom, respectively); the values of these parameters are also included in Table 1. These profiles are subsets of the corresponding profiles in Fig. 3. We see that the model and retrieved total r_{eff} values agree within 0.5 μm for four points out of six, within 1 μm for another point, while the worst agreement is within 2 μm for a single point. The difference in v_{eff} is generally within 0.05 (with the exception of one point where it is 0.13) with systematic overestimation of LES values in the RSP retrievals.

The normalized LES (blue) and RSP (red) droplet area distributions (the latter obtained using the RFT technique described above) at the six selected points are presented in Fig. 7. These plots indicate that the LES DADs have two separate modes (especially pronounced above 2-km altitude, while still detectable at lower heights) and this bimodality is accurately captured in the virtual RSP observations. For both RSP and LES DADs we used the mode-decomposition technique introduced by Alexandrov et al. (2015) to quantitatively estimate the parameters (r_{eff} and v_{eff}) of each of the modes and also the relative weights of them in the total DSDs. This method is based on properties of gamma distribution, and the assumption that each DSD mode has gamma-distribution shape has been shown to be adequate. [Note that, as in our previous publications, we plot droplet area distributions (since this is what the RFT yields), while the presented r_{eff} and v_{eff} values are for the corresponding droplet number size distributions (called DSDs throughout the paper), same that appear in physical modeling or in situ measurements.] The DSD mode-decomposition technique was designed for high-resolution smooth RFT outputs, so its application to coarse-resolution LES DADs requires linear interpolation to a denser grid and yields lower accuracy. Another reason for the differences between RSP retrievals and the actual LES DSD parameters is contribution of multiple LES grid points into each RSP measurement (given the heterogeneity of the microphysical properties in the cloud).

Fig. 8 presents a comparison of the profiles of the bimodal DSD parameters derived from the LES distributions (blue) and RSP-RFT DSD

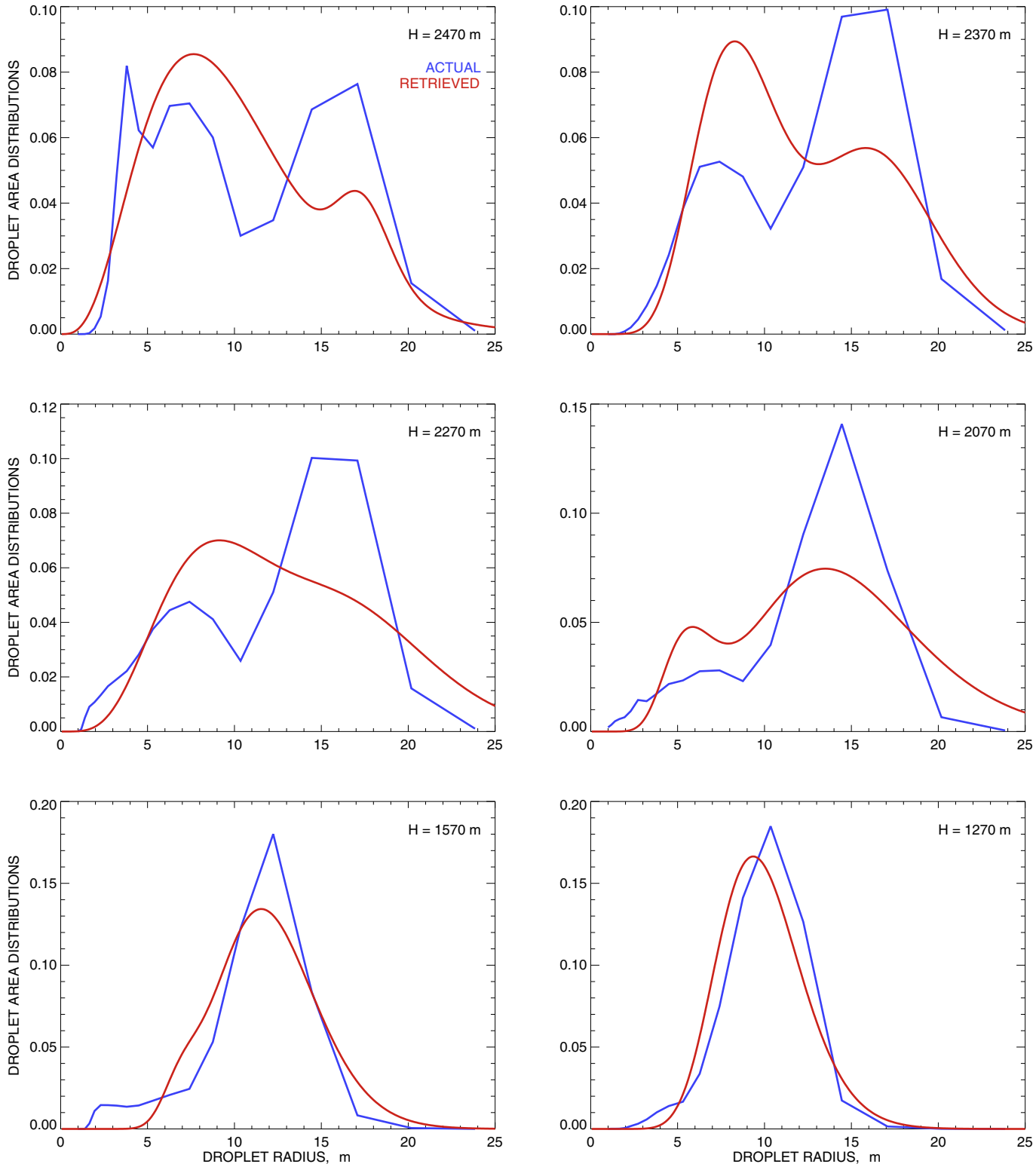

Fig. 7. Comparison between droplet area distributions derived from the virtual RSP observations (red) using RFT (with subsequent gamma-mode fit) and their actual LES-model counterparts (blue) at six grid points selected in Fig. 6 (top). (For interpretation of the references to colour in this figure legend, the reader is referred to the web version of this article.)

retrievals (red): modes' effective radii (top), effective variances (middle), and relative weights of the modes in the respective total DSDs (bottom); the values of these parameters are also included in Table 1. The data points corresponding to the smaller-size (activation) mode (Mode 1, here and in Table 1) are depicted by diamonds connected by dashed lines, while those corresponding to the larger-size (advection) mode (Mode 2, here and in Table 1) are shown by triangles connected by solid lines.

We see from Fig. 8 and Table 1 that the LES and RSP values of the advection-mode r_{eff} are in quite good agreement: within 0.5 μm for

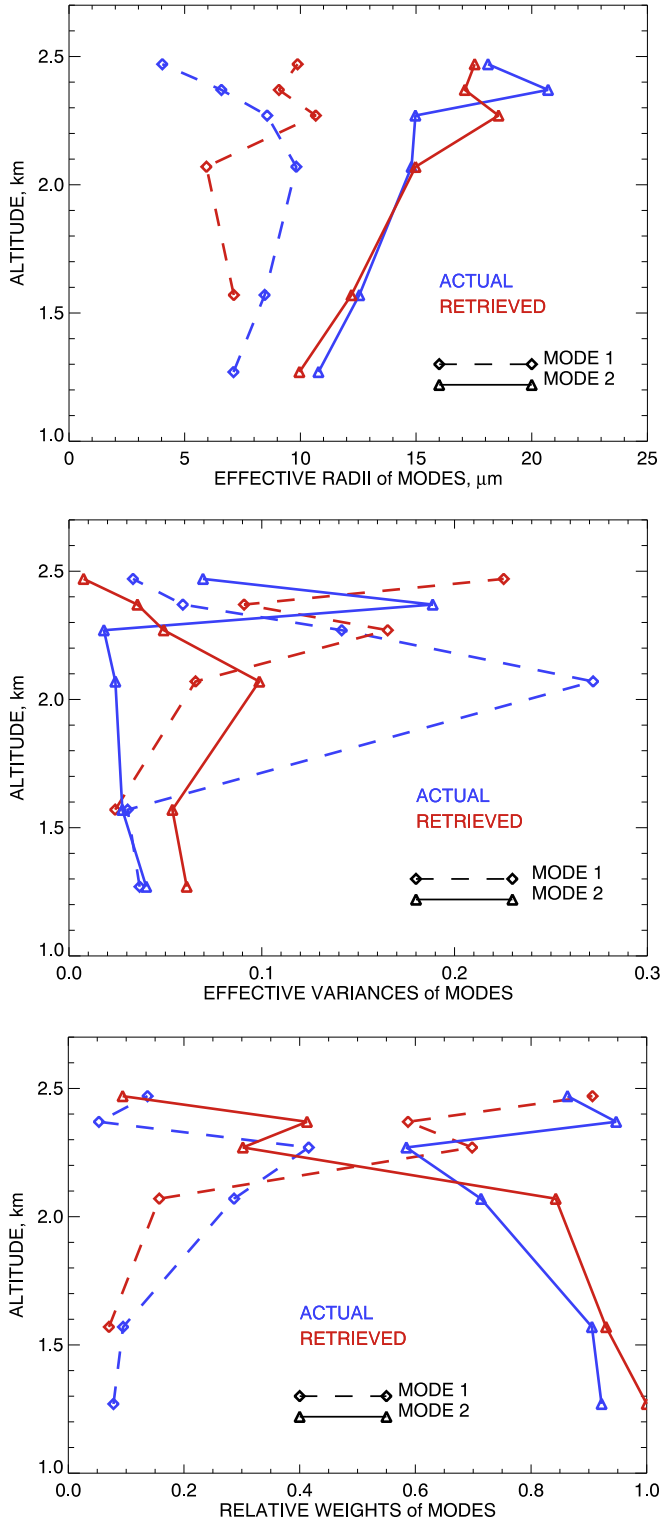

Fig. 8. Comparison between virtual-RSP retrievals and actual LES-model bimodal DSD parameters (LES in blue, RSP in red) at the six sampled points from Fig. 6 (top). Here Mode 1 is smaller in radius activation mode and Mode 2 is the larger-size advection mode. Top: profiles of the effective radii of the two modes. Middle: profiles of the effective variances. Bottom: profiles of relative weights of the modes in the total DSDs. The values of the parameters plotted here are also presented in Table 1. (For interpretation of the references to colour in this figure legend, the reader is referred to the web version of this article.)

three points out of six, within 1 μm for another point, while the worst agreement is within 4 μm for two points (the absolute difference being 1.5 μm on average). The average absolute difference in Mode-2 v_{eff} is 0.06 (0.04 if a single outlier point removed). The retrievals (and also determination from LES DSDs) of the parameters of the weaker smaller-size Mode 1 are less certain with the average absolute difference of 3 μm in r_{eff} and 0.1 in v_{eff} (mostly due to two outlier points with $v_{\text{eff}} > 0.2$, for the other three points Δv_{eff} is within 0.03); note that this mode has not been detected by RSP at the bottom point. The profiles of the weights of the two modes in Fig. 8 (bottom) show some qualitative similarities and differences between LES and RSP values. The activation mode is present throughout both RSP and LES profiles (except the bottom point in the RSP retrievals), and its rising weight from cloud bottom to 2.3-km altitude is common for the actual and observed DSDs. However, at and above this altitude the actual and observed trends in mode weighting become different. In the RSP profile the activation mode becomes dominant at 2.3 km (where its weight exceeds 50%) and continues to grow in weight up to 90% at cloud top. For the LES DSDs, on the other hand, the trend turns back into an increase in weight of the advected mode, which remains dominant throughout the entire altitude range (with 86% at cloud top). The difference in the mode weighting between the LES model output and the observations (also clearly seen in Fig. 7) can be caused by scattering events in 3D RT simulation that occur further outside of our cloud "boundary" than the aggregation point.

5. Conclusions

In this study we have explored for the first time the possibility of combining previously-developed micro- and macro-physical retrievals from the observations by the Research Scanning Polarimeter. Being a high-angular-resolution along-track airborne scanner with high radiometric and polarimetric accuracy, this instrument makes measurements facilitating retrievals of both cloud droplet size distributions and cloud shape. We demonstrated using simulated data that combination of these two types of retrievals can provide a vertical profile (along cloud side) of droplet size distribution parameters, or DSDs shapes themselves. Development of this technique allows the RSP, a passive sensor, to complement vertically resolved measurement information content from commonly-used active remote-sensing instruments, such as cloud radars. We also demonstrated that in addition to the integral characteristics of droplet size distributions (effective radius and variance), the RSP observations can reveal (by means of the Rainbow Fourier Transform) the detailed structure of DSD shape as it evolves with altitude. These virtual RSP observations identified two co-exiting populations of cloud droplets matching those present in the initial LES dataset. These populations are assumed to be related to processes of updraft-based condensation droplet growth, as well as secondary activation of droplets (caused by either updraft or entrainment) mostly pronounced near cloud top. Thus, the presented profiling technique opens the way to process-oriented remote sensing based on the RSP measurements.

The simulations in this study were made for a towering cumulus cloud (Tcu, also called cumulus congestus). This type of cloud is interesting from general remote-sensing point of view because of its vast vertical extent and, thus, expectation of diverse variety of microphysical properties to be observed. The practical incentive to focus on Tcu clouds at this time is driven by the recent Cloud, Aerosol and Monsoon Processes Philippines Experiment (CAMP^{2}Ex) conducted in August – September 2019. Some recommendations for flight configuration optimal for our profile retrievals are presented in Appendix A. We look forward to use the described cloud profiling algorithm for analysis of real RSP measurements made during CAMP^{2}Ex and for validation of our retrievals using in situ and lidar data. We will also study how the cloud shape estimation using "cutout" technique compares (and possibly can be combined) with our standard stereo block-correlation method for determination of cloud-top altitude.

Declaration of Competing Interest

The authors declare that they have no known competing financial interests or personal relationships that could have appeared to influence the work reported in this paper.

Acknowledgments

This research was funded by the NASA Radiation Sciences Program managed by Hal Maring and NASA grant NNH16ZDA001N-CAMP2EX. We are indebted to Z. Wang for development of MSCART 3D radiative transfer code and C. Emde whose simulations were used during development of our profiling techniques.

Appendix A. Optimal viewing geometry for cloud profile retrievals

The geometry of cloud profile observations by the RSP is outlined in Fig. A.1 (left): there θ is the viewing angle with its maximal value $\theta_{\max}$, θ_s is the solar zenith angle, and θ_t is the viewing angle corresponding to the line tangent to the cloud surface at the aggregation point (red dot). For RSP mounted on the NASA P−3B aircraft, as will be the case for CAMP^{2}Ex, $\theta_{\max}$ will be about 60° in the backward direction and about 45° in the forward direction. As always, the widest angular range in the rainbow region can be achieved when the measurements are made in the principal plane with the sun being directly in front or behind the aircraft. The scattering angle γ in the principle plane is defined as

$$\gamma = 180° - |\theta - \theta_s|, \tag{A.1}$$

or equivalently

$$\gamma = 180° - \theta + \theta_s, \quad \text{when } \theta > \theta_s, \tag{A.2}$$

$$\gamma = 180° + \theta - \theta_s, \quad \text{when } \theta < \theta_s. \tag{A.3}$$

If $\theta_s > \theta_t$ the aggregation point is illuminated (bright), otherwise it is in the shadow. If $\theta > \theta_t$ this point is observed by the RSP, otherwise it is blocked by other parts of the cloud. While $\theta = \theta_s$ corresponds to backscatter direction ($\gamma = 180°$), the rainbow generally can be observed on both sides of this angle: for $\theta \in [\theta_t, \theta_s]$ and for $\theta \in [\theta_s, \theta_{\max}]$. The corresponding scattering angle ranges are

$$\gamma \in [180° + \theta_t - \theta_s,\ 180°] \quad \text{for } \theta \in [\theta_t,\ \theta_s], \tag{A.4}$$

$$\gamma \in [180° - \theta_{\max} + \theta_s,\ 180°] \quad \text{for } \theta \in [\theta_s,\ \theta_{\max}]. \tag{A.5}$$

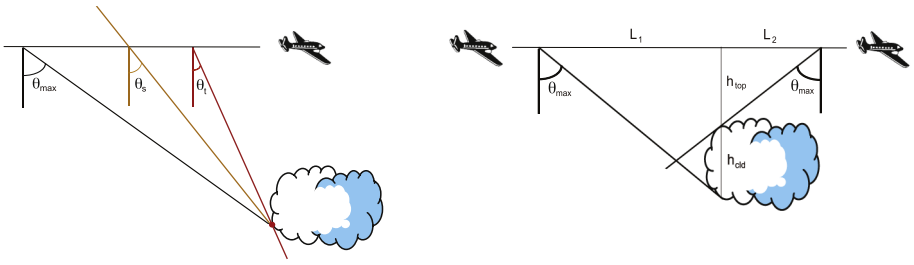

Fig. A.1. The geometry of cloud profile observations. Left: definitions of the angles: θ is the viewing angle with its maximal value $\theta_{\max}$ (60° or 45°), θ_s is the solar zenith angle, and θ_t is the viewing angle corresponding to the line tangent to the cloud surface at the aggregation point (red dot). Right: relationship between heights and distances for optimal retrieval of cloud profile. Here h_{top} is the the hight of the aircraft above cloud top, h_{cld} is the cloud thickness, L_1 and L_2 are lengths of the respective parts of the flight leg before and after crossing the cloud edge (grey line). (For interpretation of the references to colour in this figure legend, the reader is referred to the web version of this article.)

In the rainbow range $\gamma \in [135°, 165°]$. While the backscatter direction is always available for observation, there is no problem sampling the larger-angle end of the rainbow range, however, observations at smaller angles (starting at 135°) may not always be available. Requirement of availability of these measurements imposes the following conditions on the solar zenith angle θ_s:

$$180° + \theta_t - \theta_s < 135°, \quad \text{thus,} \quad \theta_s > 45° + \theta_t \tag{A.6}$$

for $\theta \in [\theta_t, \theta_s]$ (low sun), and

$$180° - \theta_{\max} + \theta_s < 135°, \quad \text{thus,} \quad \theta_s \in [\theta_t,\ \theta_{\max} - 45°] \tag{A.7}$$

for $\theta \in [\theta_s, \theta_{\max}]$ (high sun). For $\theta_{\max} = 60°$ (when $\theta \in [\theta_s, 60°]$) the high-sun interval is $\theta_s \in [\theta_t, 15°]$. This means that in this case measurements should be made right around noon for cloud points with $\theta_t < 15°$. In both low- and high-sun observation frameworks it is easier to achieve the desired outcome when $\theta_t \le 0$ (Δ-shaped clouds) than when $\theta_t > 0$ (∇-shaped clouds).

Fig. A.1 (right) demonstrates that in order to fully exploit the RSP's angular range ($\pm\,\theta_{\max}$ from nadir direction) for observations along cloud side the start of the remote sensing flight leg should be at least at the distance

$$L_0 = (h_{\text{top}} + h_{\text{cld}})\ \tan\theta_{\max} \tag{A.8}$$

from the cloud edge to be profiled (here h_{top} is the the hight of the aircraft above cloud top, h_{cld} is the cloud thickness), while the end of the leg should be further than

$$L_1 = h_{\text{top}}\ \tan\theta_{\max} \tag{A.9}$$

from the cloud edge. We see from Fig. A.1 (right) and Eqs. (A.8) and (A.9) that the observations constraining cloud bottom and top are made at the distances from the cloud that increase with the aircraft altitude h_{top} above cloud top. Observations made from large distance can be affected by various factors, such as poor visibility due to aerosols, fluctuations in flight speed and direction, and presence of other clouds that may obscure the cloud of interest. Observational altitude of 1.5 km above cloud top used in the simulated example described in this paper has been demonstrated to

be sufficiently low for accurate determination of cloud shape and microphysical profiles. Thus, we recommended this and lower altitudes for practical use.

For practical recommendations in the case of $\theta_{max} = 60^{\circ}$ we assume that $\tan\theta_{\max} \approx 1.73 \approx 2$ and replace $h_{\text{top}} + h_{\text{cld}}$ in Eq. (A.8) with the aircraft altitude above ground. These recommendations then are the following:

- Remote sensing leg at altitude of about 1.5 km or less above cloud top. 500-m altitude seems particularly suitable for CAMP^{2}Ex cloud scene and flight conditions.
- Straight and leveled legs in the principal plane approaching the cloud at either the illuminated or shadowy side.
- If the aircraft approaches from the bright side of the cloud, the start point of the leg should be at a distance from the illuminated cloud edge (to be profiled) that is more or equal to twice the aircraft altitude. The end point of the leg in this case should be at a distance more or equal to twice the distance between aircraft altitude and cloud top.
- If the aircraft approaches the cloud from shadowy side (as the RSP makes measurements in both forward and backward directions) the previous statement should be appropriately reversed ("start" ↔ "end"). This flight configuration will be preferable during CAMP^{2}Ex because the RSP mounted on the NASA P−3B aircraft has wider angular range in backward direction than in forward one.

References

Ackerman, A.S., Kirkpatrick, M.P., Stevens, D.E., Toon, O.B., 2004. The impact of humidity above stratiform clouds on indirect aerosol climate forcing. Nature 432, 1014–1017.

Ackerman, A.S., Fridlind, A.M., Grandlin, A., Dezitter, F., Weber, M., Strapp, J.W., Korolev, A., 2015. High ice water content at low radar reflectivity near deep convection – part 2. Evaluation of microphysical pathways in updraft parcel simulations. Atmos. Chem. Phys. 15, 11729–11751.

Alexandrov, M.D., Cairns, B., Emde, C., Ackerman, A.S., van Diedenhoven, B., 2012a. Accuracy assessments of cloud droplet size retrievals from polarized reflectance measurements by the research scanning polarimeter. Remote Sens. Environ. 125, 92–111.

Alexandrov, M.D., Cairns, B., Mishchenko, M.I., 2012b. Rainbow Fourier transform. J. Quant. Spectrosc. Radiat. Transf. 113, 2521–2535.

Alexandrov, M.D., Cairns, B., Wasilewski, A.P., Ackerman, A.S., McGille, M.J., Yorks, J.E., Hlavka, D.L., Platnick, S.E., Arnold, G.T., van Diedenhoven, B., Chowdhary, J., Ottaviani, M., Knobelspiesse, K.D., 2015. Liquid water cloud properties during the Polarimeter Definition Experiment (PODEX). Remote Sens. Environ. 169, 20–36.

Alexandrov, M.D., Cairns, B., van Diedenhoven, B., Ackerman, A.S., Wasilewski, A.P., McGill, M.J., Yorks, J.E., Hlavka, D.L., Platnick, S.E., Arnold, G.T., 2016a. Polarized view of supercooled liquid water clouds. Remote Sens. Environ. 181, 96–110.

Alexandrov, M.D., Cairns, B., Emde, C., Ackerman, A.S., Ottaviani, M., Wasilewski, A.P., 2016b. Derivation of cumulus cloud dimensions and shape from the airborne measurements by the Research Scanning Polarimeter. Remote Sens. Environ. 177, 144–152.

Alexandrov, M.D., Cairns, B., Sinclair, K., Wasilewski, A.P., Ziemba, L., Crosbie, E., Moore, R., Hair, J., Scarino, A.J., Hu, Y., Stamnes, S., Shook, M.A., Chen, G., 2018. Retrievals of cloud droplet size from the research scanning polarimeter data: Validation using in situ measurements. Remote Sens. Environ. 210, 76–95.

Barker, H., Goldstein, R., Stevens, D., 2003. Monte Carlo simulation of solar reflectances for cloudy atmospheres. J. Atmos. Sci. 60, 1881–1894.

Boucher, O., Randall, D., Artaxo, P., Bretherton, C, Feingold, G., Forster, P., Kerminen, V.-M., Kondo, Y., Liao, H., Lohmann, U., Rasch, P, Satheesh, S., Sherwood, S., Stevens, B., Zhang, X, 2013. Clouds and aerosols. In: Stocker, T., Qin, D., Plattner, G.-K., Tignor, M., Allen, S., Boschung, J. ... Midgley, P. (Eds.), Climate Change 2013: The Physical Science Basis. Contribution of Working Group I to the Fifth Assessment Report of the Intergovernmental Panel on Climate Change. Cambridge University Press, pp. 571–657.

Bréon, F.M., Doutriaux-Boucher, M., 2005. A comparison of cloud droplet radii measured from space. IEEE Trans. Geosci. Remote Sens. 43, 1796–1805.

Bréon, F.-M., Goloub, P., 1998. Cloud droplet effective radius from spaceborne polarization measurements. Geophys. Res. Lett. 25, 1879–1882.

Buras, R., Mayer, B., 2011. Efficient unbiased variance reduction techniques for Monte Carlo simulations of radiative transfer in cloudy atmospheres: the solution. J. Quant. Spectrosc. Radiat. Transf. 112, 434–447.

Cairns, B., Russell, E.E., Travis, L.D., 1999. Research scanning polarimeter: Calibration and ground-based measurements. In: Goldstein, D.H., Chenault, D.B. (Eds.), Polarization: Measurement, Analysis, and Remote Sensing, pp. 186–197 volume 3754 of Proc. SPIE.

Emde, C., Buras, R., Mayer, B., Blumthaler, M., 2010. The impact of aerosols on polarized sky radiance: model development, validation, and applications. Atmos. Chem. Phys. 10, 383–396.

Emde, C., Barlakas, V., Cornet, C., Evans, F., Wang, Z., Labonotte, L.C., Macke, A., Mayer, B., Wendisch, M., 2018. IPRT polarized radiative transfer model intercomparison project Three-dimensional test cases (phase B). J. Quant. Spectrosc. Radiat. Transf. 209, 19–44.

Flato, G., Marotzke, J., Abiodun, B., Braconnot, P., Chou, S., Collins, W., Cox, P., Driouech, F., Emori, S., Eyring, V., Forest, C., Gleckler, P., Guilyardi, E., Jakob, C., Kattsov, V., Reason, C., Rummukainen, M., 2013. Evaluation of climate models. In: Stocker, T., Qin, D., Plattner, G.-K., Tignor, M., Allen, S., Boschung, J. ... Midgley, P. (Eds.), Climate Change 2013: The Physical Science Basis. Contribution of Working Group I to the Fifth Assessment Report of the Intergovernmental Panel on Climate Change. Cambridge University Press, pp. 741–866.

Fridlind, A.M., Li, X., Wu, D., van Lier-Walqui, M., Ackerman, A.S., Tao, W.-K., McFarquhar, G.M., Wu, W., Dong, X., Wang, J., Ryzhkov, A., Zhang, P., Poellot, M.R., Neumann, A., Tomlinson, J.M., 2017. Derivation of aerosol profiles for MC3E convection studies and use in simulations of the 20 May squall line case. Atmos. Chem. Phys. 17, 5947–5972.

Hansen, J.E., Travis, L.D., 1974. Light scattering in planetary atmospheres. Space Sci. Rev. 16, 527–610.

Iwabuchi, H., 2006. Efficient Monte Carlo methods for radiative transfer modeling. J. Atmos. Sci. 63, 2324–2339.

Iwabuchi, H., Suzuki, T., 2009. Fast and accurate radiance calculations using truncation approximation for anisotropic scattering phase functions. J. Quant. Spectrosc. Radiat. Transf. 110, 1926–1939.

Johnson, R.H., Rickenbach, T.M., Rutledge, S.A., Ciesielski, P.E., Schubert, W.H., 1999. Trimodal characteristics of tropical convection. J. Clim. 12, 2397–2418.

Kirkpatrick, M.P., Ackerman, A.S., Stevens, D.E., Mansour, N.N., 2006. On the application of the dynamic Smagorinsky model to large-eddy simulations of the cloud-topped atmospheric boundary layer. J. Atmos. Sci. 64, 526–546.

Ladino, L.A., Korolev, A., Heckman, I., Wolde, M., Fridlind, A.M., Ackerman, A.S., 2017. On the role of ice-nucleating aerosol in the formation of ice particles in tropical mesoscale convective systems. Geophys. Res. Lett. 44, 1574–1582.

Lasher-Trapp, S.G., Cooper, W.A., Blyth, A.M., 2005. Broadening of droplet size distributions from entrainment and mixing in a cumulus cloud. Q. J. R. Meteorol. Soc. 131, 195–220.

Li, W., Luo, C., Wang, D., Lei, T., 2010. Diurnal variations of precipitation over the South China Sea. Meteorog. Atmos. Phys. 109, 33–46.

Mayer, B., 2009. Radiative transfer in the cloudy atmosphere. Eur. Phys. J. Conf. 1, 75–99.

Miller, D.J., Zhang, Z., Ackerman, A.S., Platnick, S., Baum, B.A., 2016. The impact of cloud vertical profile on liquid water path retrieval based on the bispectral method: a theoretical study based on large-eddy simulations of shallow marine boundary layer clouds. J. Geophys. Res. 121, 4122–4141.

Mishchenko, M.I., Travis, L.D., Lacis, A.A., 2006. Multiple Scattering of Light by Particles: Radiative Transfer and Coherent Backscattering. Cambridge University Press.

Nakajima, T., King, M.D., 1990. Determination of the optical thickness and effective particle radius of clouds from reflected solar radiation measurements. Part I: theory. J. Atmos. Sci. 47, 1878–1893.

Platnick, S., 2000. Vertical photon transport in cloud remote sensing problems. J. Geophys. Res. 105, 22919–22935.

Segal, Y., Pinsky, M., Khain, A., Erlick, C., 2003. Thermodynamic factors influencing bimodal spectrum formation in cumulus clouds. Atmos. Res. 66, 43–64.

Shang, H., Chen, L., Breon, F.-M., Letu, H., Li, S., Wang, Z., Su, L., 2015. Impact of cloud horizontal inhomogeneity and directional sampling on the retrieval of cloud droplet size by the POLDER instrument. Atmos. Meas. Tech. 8, 4931–4945.

Shang, H., Letu, H., Bron, F.-M., Riedi, J., Ma, R., Wang, Z., Nakajima, T.Y., Wang, Z., Chen, L., 2019. An improved algorithm of cloud droplet size distribution from POLDER polarized measurements. Remote Sens. Environ. 228, 61–74.

Sheffield, A.M., Saleeby, S.M., van den Heever, S.C., 2015. Aerosol-induced mechanisms for cumulus congestus growth. J. Geophys. Res. Atmos. 120, 8941–8952.

Sinclair, K., van Diedenhoven, B., Cairns, B., Yorks, J., Wasilewski, A., McGill, M., 2017. Remote sensing of multiple cloud layer heights using multi-angular measurements. Atmos. Meas. Tech. 10, 2361–2375.

Stevens, D.E., Bretherton, C.S., 1996. A forward-in-time advection scheme and adaptive multilevel flow solver for nearly incompressible atmospheric flow. J. Comput. Phys. 129, 284–295.

Stevens, D.E., Bell, J.B., Almgren, A.S., Beckner, V.E., Rendleman, C.A., 2000. Small-scale processes and entrainment in a stratocumulus marine boundary layer. J. Atmos. Sci. 57, 567–581.

Stevens, D.E., Ackerman, A.S., Bretherton, C.S., 2002. Effects of domain size and numerical resolution on the simulation of shallow cumulus convection. J. Atmos. Sci. 59, 3285–3301.

Waite, M.L., Khouider, B., 2010. The deepening of tropical convection by congestus preconditioning. J. Atmos. Sci. 67, 2601–2615.

Wang, Z., Cui, S., Yang, J., Gao, H., Liu, C., Zhang, Z., 2017. A novel hybrid scattering order-dependent variance reduction method for Monte Carlo simulations of radiative transfer in cloudy atmosphere. J. Quant. Spectrosc. Radiat. Transf. 189, 283–302.

Zhang, Z., Ackerman, A.S., Feingold, G., Platnick, S., Pincus, R., Xue, H., 2012. Effects of cloud horizontal inhomogeneity and drizzle on remote sensing of cloud droplet effective radius: Case studies based on large-eddy simulations. J. Geophys. Res. 117, D19208.